A sandwich-like heterostructure of TiO_2 nanosheets with MIL-100(Fe): A platform for efficient visible-light-driven photocatalysis

Xin Liu, Rui Dang, Wenjun Dong*, Xiubing Huang, Jia Tang, Hongyi Gao, Ge Wang*

School of Materials Science and Engineering, University of Science and Technology Beijing, Beijing 100083, China

ABSTRACT

Hierarchical heterostructures with specific compositions, morphology and functionalities are important for applications in many fields such as catalysis, energy storage and conversion. Herein, hierarchical sandwich-like heterostructures were prepared by a self-assembly method of growing MIL-100(Fe) on host two dimensional (2D) TiO_2 nanosheets (TiO_2NS). The introduction of porous MIL-100(Fe) on TiO_2NS improves the adsorption ability of nanocomposites owing to the porous tunnel adsorbing organic molecules and high surface area. In addition, the interfaces of TiO_2NS and MIL-100(Fe) provide platforms for rapid photoexcited electrons transfer and enhance the photocatalytic activity of TiO_2NS@MIL-100(Fe) nanocomposites. The resulting sandwich-like TiO_2NS@MIL-100(Fe) nanocomposites with enhanced adsorption ability and superior separation of photogenerated electron-hole pairs exhibited improved photoactivity toward degradation of methylene blue dye (MB) under visible light ($\lambda \geq 420$ nm). TiO_2NS@MIL-100(Fe) nanocomposites offer an useful platform to integrate photocatalytic semiconductor and porous MOFs into hierarchical nanostructures with high surface areas and efficient electrons transfer for enhanced photocatalytic performance.

© 2017 Elsevier B.V. All rights reserved.

1. Introduction

Titanium dioxide (TiO_2), an efficient semiconducting photocatalyst, has received great attention due to its high structural stability, strong oxidizing ability and low toxicity, and has been extensively employed for water splitting, energy storage, and organic pollutant degradation [1–8]. In particular, two dimensional (2D) TiO_2 nanosheets (TiO_2NS), containing high energy {001} facets and a mass of active surface sites, exhibit high surface reaction kinetics and enhanced photocatalytic properties [9,10]. However, issues remain a hindrance to the large-scale commercialisation of pure TiO_2NS. For instance, the vulnerability of pure TiO_2NS to aggregate, results in reduced surface area and poor adsorption ability. The fast recombination of photoexcited electron-hole pairs on the surface of aggregated TiO_2NS significantly reduces the efficiency of the photocatalytic reaction [7]. Recently, several methods were developed to extend the light-response window and improve the photocatalytic efficiency of TiO_2NS, such as loading with noble metals [11–13], and

incorporation with carbon materials [14,15]. The characteristic low surface areas of the yield TiO_2NS-based photocatalysts elicit inefficient molecular adsorption ability and low photocatalytic reaction dynamics. So far, it is rare to see significant advances in both the adsorption property and photocatalytic efficiency of TiO_2NS-based photocatalysts.

Metal-organic frameworks (MOFs), an emerging class of 3D porous crystalline frameworks possessing high surface areas and well-ordered pore size, have demonstrated a great applied potential in gas storage, adsorption and catalysis [16–19]. Notably, some particular MOF species such as Ti(IV)MOFs [20–23], Fe-MOFs [24–28], Zr-MOFs [29–32] and Zn-MOFs [33], could perform promising photocatalytic behaviour through light irradiation, which is ascribed to the readiness of their electrons being excited from HOMO (oxygen and/or nitrogen orbitals) to LUMO (metal cluster). However, low efficient excitons generation and charge separation of MOFs lead to low quantum efficiency in photocatalytic reactions [34], Hence, it could be a plausible strategy to improve the quantum efficiency of MOFs by means of the incorporation of MOFs with inorganic semiconductors [35,36]. Of the existing semiconductor@MOFs heterostructures, TiO_2@MOFs outperform their counterparts in terms of a synergistic effect of high adsorption, and efficient charge excitation and transfer. For example,

* Corresponding authors.
E-mail addresses: wdong@ustb.edu.cn (W. Dong), gewang@mater.ustb.edu.cn (G. Wang).

the MOFs@TiO_2 with core-shell nanostructures photocatalyze the gaseous reactions to a great magnitude [37], given the characteristic functionalities of the microporous shells (excitons generator) and the microporous core (gas molecules hunter). A heterostructure of mesoporous MOFs incorporated with amorphous TiO_2, inhibits the recombination of photoexcited electron-hole pairs and yields a high performance of selective aerobic oxidation under sun light [38]. The interfaces between inorganic semiconductors and MOFs provide numerous favorable sites for transition of photogenerated electrons, which substantially accelerates the electron transfer and suppress electron–holes recombination in the photocatalysts [37]. The common preparation approaches, however, facilitate the formation of monodisperse photoactive TiO_2 particles exclusively on the surface of MOFs, which deactivate the favorably functional interfaces between TiO_2 particles and MOFs. In literature, it has been recognized that the mean surface energy of anatase TiO_2 follow an order of {001} (0.9 J m^{-2}) > {100} (0.53 J m^{-2}) > {101} (0.44 J m^{-2}) [39]. Chemical activity of the (001) surface is also a function of surface energy, which is key to anchor MOFs on the surface of TiO_2NS and create more functional interfaces [40]. The incorporation of the nanosheet-shaped TiO_2 containing a high number of exposed {001} facets into MOFs is expected to accelerate photogenerated electrons transfer between the created interfaces of TiO_2NS and MOFs. As such, design and building hierarchically porous structures through assembling 2D TiO_2NS with MOFs would be an ideal solution to create a large number of functional interfaces and boost photocatalytic efficiency.

Herein, a hierarchical sandwich-like TiO_2NS@MIL-100(Fe) heterostructure was developed through a self-assembled method by incorporating MIL-100(Fe) into TiO_2NS. The as-synthesized TiO_2NS@MIL-100(Fe) nanocomposites exhibit high adsorption ability and efficient photocatalytic performance to photodegrade methylene blue (MB) by radiation of visible light ($\lambda \geq 420$ nm). The high adsorption ability can be attributed to the introduction of porous MIL-100(Fe) with high surface areas into the TiO_2NS system. Meanwhile, the high number of newly-created interfaces of the TiO_2NS and MIL-100(Fe) contributes greatly to the enhancement in photocatalytic property, which accelerates photogenerated electrons transfer and facilitates the separation of electron-hole pairs. In particular, TiO_2NS with 33 wt.% MIL-100(Fe) addition presents remarkable photocatalytic activity for redox reactions. The corresponding constant of kinetics rate (0.045 min^{-1}) is approximately 2 and 45 times larger than those of MIL-100(Fe) (0.019 min^{-1}) and pure TiO_2NS (0.0008 min^{-1}), respectively.

2. Experimental

2.1. Synthesis of TiO_2NS and MIL-100(Fe)

TiO_2NS were prepared according to the reported procedures [41]. In brief, 25 ml of Ti(OBu)$_4$ and 5 ml of HF solution were well mixed in a dry Teflon-lined autoclave with a capacity of 100 ml,

maintained at 200 °C for 20 h, and followed by natural cooling to ambient temperature. The precipitates were collected by centrifugation, and washed with deionized water and ethanol for several times. Finally, the yielded white products were dried at 80 °C for 6 h under vacuum conditions.

MIL-100(Fe) was synthesized by the previously reported method [42]. Typically, FeCl$_3$·6H$_2$O (1 mmol, 162.2 mg), benzene-1,3,5-tricarboxylic acid (0.66 mmol, 138.7 mg) and deionized water (5 ml) were well mixed in a dry Teflon-lined autoclave with a capacity of 25 ml, maintained at 130 °C for 3 days. The reaction products were purified with deionized water (350 ml) and ethanol (350 ml) at 70 °C for 12 h, respectively. Finally, the yielded orange products were dried at 130 °C for 12 h under vacuum conditions.

2.2. Synthesis of TiO_2NS@MIL-100(Fe) nanocomposites

TiO_2NS@MIL-100(Fe) nanocomposites were synthesized by a self-assembly method [43]. The preparation process consists of three steps: (1) adsorption of Fe^{3+} ions on TiO_2NS in solution; (2) formation of MIL-100(Fe) on TiO_2NS, and (3) assembly of sandwich-like structural TiO_2NS@MIL-100(Fe) nanocomposites after successive reaction (refer to Scheme 1 for more details). To be specific, 0.1 g of pure TiO_2NS powder was dispersed in 10 ml of FeCl$_3$ ethanol solution (10 mM) under ultrasonic conditions for 30 min to suppress aggregation, stirred for 15 min, and then transferred into 10 ml of benzene-1,3,5-tricarboxylic acid ethanol solution (10 mM) in a water bath at 70 °C for 30 min. After each step, TiO_2NS were separated by vacuum filtration and washed with ethanol. After a given number of circles, the products were rinsed with ethanol, and freeze-dried under vacuum.

2.3. Characterization

X-ray diffraction (XRD) was conducted using a M21X diffractometer operated at 40 kV and 200 mA with Ni-filtered Cu Kα irradiation ($\lambda = 1.541$ Å) source. XRD spectra were recorded in a 2θ range of 2–70°. Scanning electron microscopy (SEM) images were obtained with a ZEISS SUPRA 55. Transmission electron microscopy (TEM) and high-resolution TEM (HRTEM) were utilized to reveal the structure of the samples (JEOL JEM1200EX). Elemental mapping analysis over the regions of interest was performed using energy-disperse X-ray spectrometry (EDS) equipped with TEM. Thermogravimetric analysis (TGA) was carried out using a STA 449F3 instrument under a nitrogen atmosphere. Porosity and Brunauer–Emmett–Teller (BET) surface area were measured by an AUTOSORB-1C analyser. X-ray photoelectron spectroscopy (XPS) were conducted on a Thermo escalab 250Xi system. UV–vis diffuse reflectance spectra (DRS) were recorded on a Shimadzu UV-2550. Barium sulphate (BaSO$_4$) was used as a reflectance standard. Mott–Schottky analysis was performed at a Princeton electrochemical workstation. The photocurrent measurement was conducted on a Chenhua CHI660D electrochemical workstation. Edinburgh
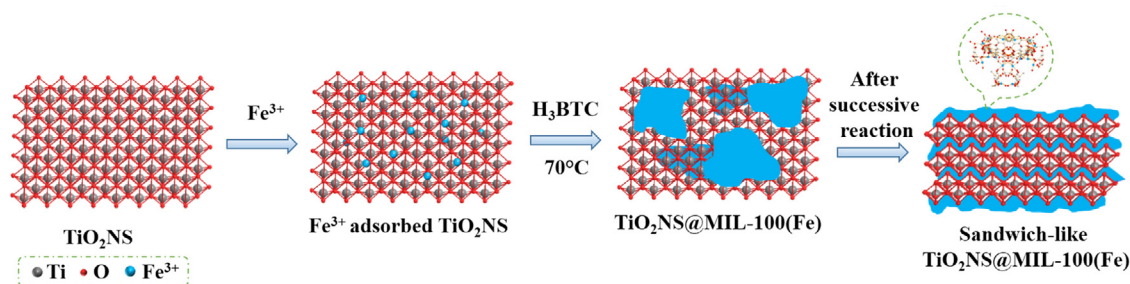
Scheme 1. Synthetic illustration of the preparation procedures for TiO_2NS@MIL-100(Fe) nanocomposites.

FL/FS900 spectrophotometer was used to obtained photoluminescence (PL) spectra.
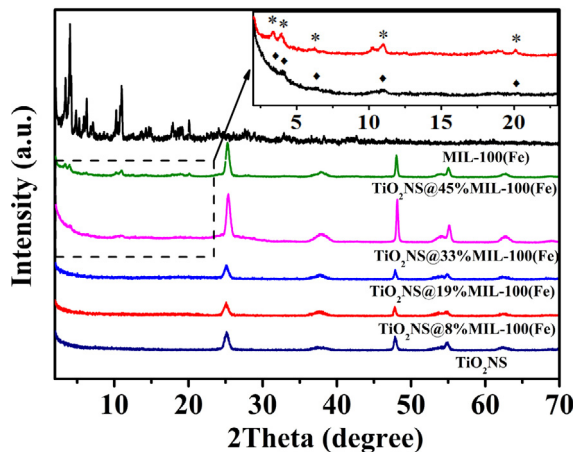
2.4. Evaluation of photocatalytic activity

Photocatalytic performance of the TiO$_2$NS@MIL-100(Fe) photocatalysts was evaluated by photodegradation of methylene blue dye (MB). 20 mg of TiO$_2$NS@MIL-100(Fe) photocatalyst and 0.2 ml hydrogen peroxide (H$_2$O$_2$) were mixed with 100 ml MB aqueous solution (50 mg l^{-1}) in a 250 ml breaker. The suspension was stirred in dark for 1 h to establish an adsorption–desorption equilibrium and followed by irradiation of visible light (420 nm $\ll \lambda \ll$ 760 nm). 3 ml MB solution were acquired at regular intervals (20 min) and the photocatalysts in the 3 ml MB solution were separated immediately by centrifuging. Variation of MB concentration was monitored by measuring the adsorption intensity at λ = 664 nm using a UV-visible spectrophotometer (UV-2550, Shimadzu).
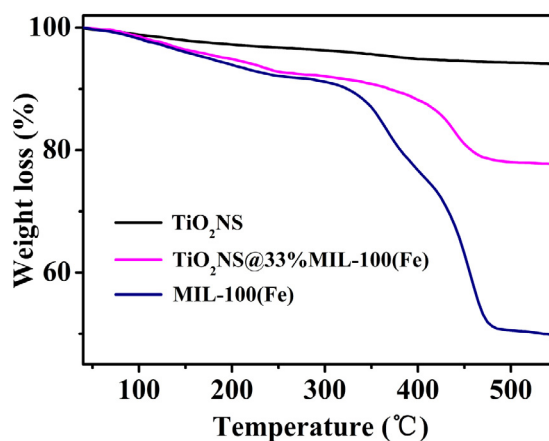
3. Results and discussion

3.1. Structural and morphological characterization

XRD pattern of bare TiO$_2$NS (Fig. 1) depicts characteristic tetragonal structure with anatase TiO$_2$ (JCPDS 21-1272) [39]. Crystallographic features of as-prepared MIL-100(Fe) are in agreement with those reported in the literature [42]. After self-assembly of MIL-100(Fe) onto TiO$_2$NS, the XRD patterns include the unique peaks are ascribed to both TiO$_2$NS and MIL-100(Fe) (e.g. 2θ = 3.5°, 4.1°, 11.0°, 25.2°). The lower self-assembly synthesis cycles leads to the formation of MIL-100(Fe) with less crystallinity but active groups, which could absorb excessive ions of precursors for further self-assembly. With the number of synthesis cycles increases, the intensity of diffraction peaks of the yielded products in the range of 2θ = 2–23° (inset in Fig. 1) elevates, indicating increasing quantity of the MIL-100(Fe) on TiO$_2$NS. The addition of MIL-100(Fe) onto TiO$_2$NS was further confirmed through thermogravimetric analysis (TGA, Fig. 2). The weight loss around 200 °C is assigned to the removal of water molecules and the desorption of organic ligand from the surfaces of the nanocrystals [44]. Collapse of the framework of MIL-100(Fe)-TiO$_2$NS occurs between 250 and 450 °C, as a result of the decomposition of carboxylic acid. When heated at 550 °C, neat TiO$_2$NS exhibit trivial decomposition due to its high heat stability, whilst a weight loss of TiO$_2$NS@33%MIL-100(Fe) 19% higher than that of neat TiO$_2$NS is evident, indicating the presence of MIL-100(Fe) on TiO$_2$NS.

Fig. 2. TGA curves of TiO$_2$NS, MIL-100(Fe) and TiO$_2$NS@33%MIL-100(Fe) nanocomposites.
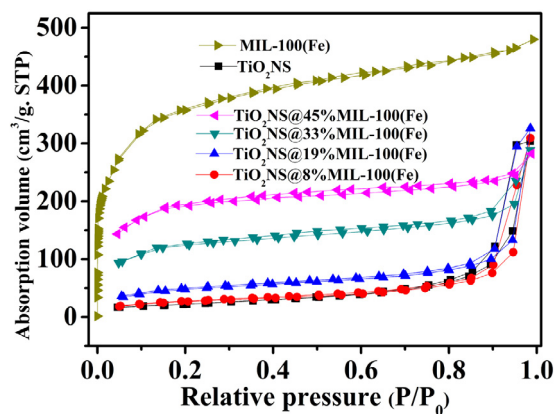
Fig. 3. N$_2$ adsorption–desorption isotherms of TiO$_2$NS, MIL-100(Fe) and TiO$_2$NS@MIL-100(Fe) nanocomposites.
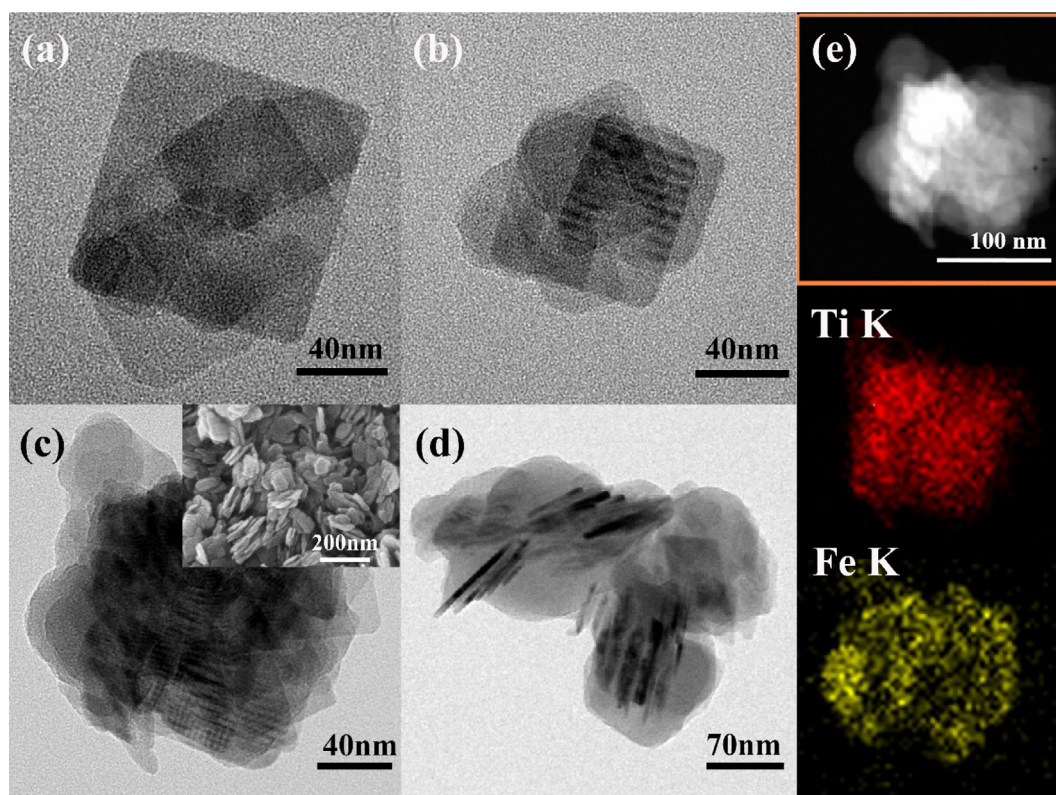
Brunauer–Emmett–Teller (BET) surface area (Fig. 3 and Table 1) were measured to reveal the porous nature of samples. The nitrogen adsorption–desorption isotherms curve for neat TiO$_2$NS sample exhibits type II isotherm, a solid evidence of mesoporous structure [10]. Moreover, the BET curves of sandwich-like TiO$_2$NS@MIL-100(Fe) nanocomposites resemble combined type I and IV isotherms with a slight desorption hysteresis, revealing the coexistence of microporosity and mesoporosity and increased nitrogen uptake capacity [37,45]. The optimized adsorption ability is further confirmed by the increase in S_{BET} of TiO$_2$NS samples with the introduction of porous MIL-100(Fe). In particular, with the quantity of added MIL-100(Fe) increasing from 0 to 33 wt.%, the BET surface area of TiO$_2$NS@MIL-100(Fe) nanocomposites increase significantly from 81.7 m^2 g^{-1} to 725.4 m^2 g^{-1}. It is expected that greater specific surface area of porous photocatalysts can adsorb more organic molecules and accelerate charge/carrier transport much greater, leading to an enhanced photocatalytic performance.

Table 1
BET surface area of TiO$_2$NS, MIL-100(Fe) and TiO$_2$NS@MIL-100(Fe) nanocomposites.

Sample	BET surface area (m^2 g^{-1})
TiO$_2$NS	81.7
TiO$_2$NS@8%MIL-100(Fe)	98.1
TiO$_2$NS@19%MIL-100(Fe)	182.5
TiO$_2$NS@33%MIL-100(Fe)	474.3
TiO$_2$NS@45%MIL-100(Fe)	725.4
MIL-100(Fe)	1669.5

Fig. 1. XRD patterns of TiO$_2$NS, MIL-100(Fe) and TiO$_2$NS@MIL-100(Fe) nanocomposites; the inset are the enlarged XRD patterns of TiO$_2$NS@33%MIL-100(Fe) and TiO$_2$NS@45%MIL-100(Fe) in the region of 2θ = 2–23°.

Fig. 4. TEM images and EDS mapping of TiO$_2$NS@wt.% MIL-100(Fe) nanocomposites: (a) 8%, (b) 19%, (c) 33%, (d) 45% and (e) mapping images of TiO$_2$NS@33%MIL-100(Fe); the inset is the FESEM image of TiO$_2$NS@33%MIL-100(Fe).

Specially, the BET surface area (98.1 m^2 g^{-1}) of TiO$_2$NS@8%MIL-100(Fe) being much lower than expected can be ascribed to the less self-assembly synthesis cycles leading to the formation of MIL-100(Fe) with less crystallinity and low surface areas, which is in agreement with the results of XRD.

FESEM and TEM images illustrate the influence of the MIL-100(Fe) introduction on the morphological characteristics of TiO$_2$NS samples (Fig. 4, Figs. S1 and S2). Neat TiO$_2$NS exhibit well-defined rectangle and single sheet-shaped structures with an average edge length of *ca.* 60–100 nm. The exposed flat and square surface is determined as {001} facets (Fig. S2) [39]. MIL-100(Fe) was successfully loaded on the surface of TiO$_2$NS while the multi-layered integrated structures and the sandwich-like cross-section of TiO$_2$NS@MIL-100(Fe) were well established (Figs. S3b, S3c, Fig. 4a–d). Moreover, the as-formed TiO$_2$NS@MIL-100(Fe) nanocomposites exhibit the clear interfaces between TiO$_2$NS and MIL-100(Fe), and it is apparent that the numbers of layers and interfaces of TiO$_2$NS and MIL-100(Fe) increases as a function of the circles of synthesis procedures. However, the incorporation of excessive MIL-100(Fe) on TiO$_2$NS reinforces the self-nucleation and aggregation of MIL-100(Fe) (Fig. 4d). EDS elemental mapping (Fig. 4e) further confirms that TiO$_2$NS were decorated with amorphous and porous MIL-100(Fe).

Chemical composition and binding status of neat TiO$_2$NS and TiO$_2$NS@33%MIL-100(Fe) were measured by XPS. The survey spectrum (Fig. 5a) signifies the presence of Ti, Fe, O, C and F. Notably, the F 1s peak of 684.5 eV is an evidence of fluorination of TiO$_2$NS [46]. Regarding both samples, the characteristics binding energy at approximately 458.8 and 464.3 eV can be assigned to the Ti 2p$_{3/2}$ and Ti 2p$_{1/2}$, respectively, which correspond to Ti^{4+} in a tetragonal structure (Fig. S5) [47]. The peaks of Fe 2p$_{3/2}$ and Fe 2p$_{1/2}$ (Fig. 5b) at approximately 711.6 and 724.1 eV, respectively, discovers the presence of Fe element in the form of Fe^{3+} [48].

Optical responses of the as-prepared photocatalysts were conducted on a UV–vis DRS. No detectable adsorption for neat TiO$_2$NS in the visible region is attributed to its large band gap. The optical responses of MIL-100(Fe) in UV region is assigned to "π–π" transitions of organic ligands, while the absorption responses in visible light region is probably related to the optical transition of ligand-to-metal charge transfer (LMCT) [24,25] or direct excitation of the Fe-O clusters [27] (Fig. 6). In addition, quantity of the loaded MIL-100(Fe) plays a significant role in the light-absorption properties of TiO$_2$NS@MIL-100(Fe) nanocomposites. An enlarged view of the range of λ = 350–500 nm (inset of Fig. 6a) depicts the enhanced adsorption properties of MIL-100(Fe)-TiO$_2$NS samples. The intercept of the tangents of $(Ahv)^2$ *vs.* photon energy was used to estimate the band-gap energy (Fig. 6b), indicating that the addition of MIL-100(Fe) can induce visible light response to TiO$_2$NS@MIL-100(Fe) nanocomposites.

3.2. Photocatalytic activities

Adsorption and photodegradation of MB with respect to neat TiO$_2$NS, MIL-100(Fe) and TiO$_2$NS@MIL-100(Fe) nanocomposites were conducted through measuring the maximum absorbance intensity at λ$_{max}$ = 664 nm (Fig. 7). It is obvious that the adsorption capacity of TiO$_2$NS@MIL-100(Fe) nanocomposites is a function of the quantity of loaded MIL-100(Fe) onto TiO$_2$NS (Fig. 7a). Furthermore, decolorization of MB was negligible under visible light without photocatalyst, whilst the most significant decolorization of MB underwent with TiO$_2$NS@33%MIL-100(Fe). Such an enhanced photoelectrons transfer could be ascribed to the interfaces between TiO$_2$NS and MIL-100(Fe) in the sandwich-like structure. In order to understand adsorption and photocatalytic reaction kinetics of
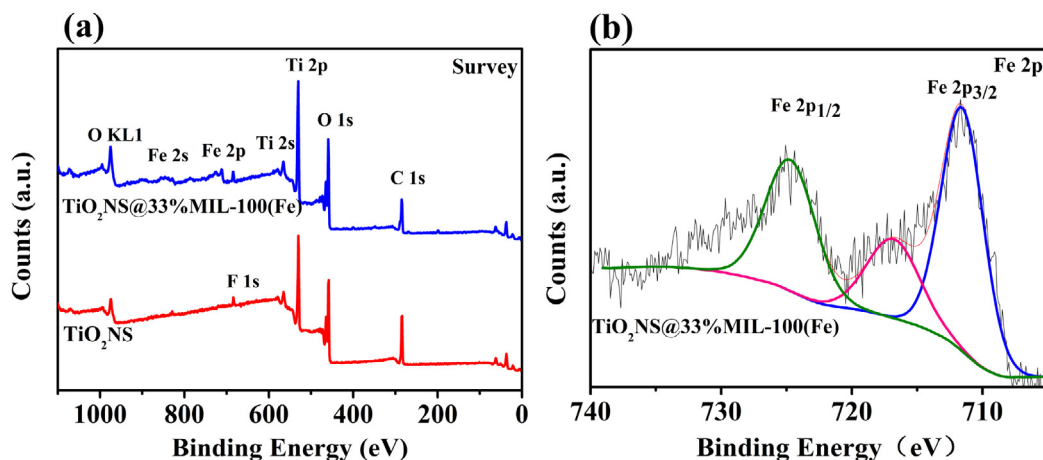
Fig. 5. XPS patterns measurements of neat TiO$_2$NS and TiO$_2$NS@33%MIL-100(Fe): (a) survey and (b) Fe 2p binding energy spectra.
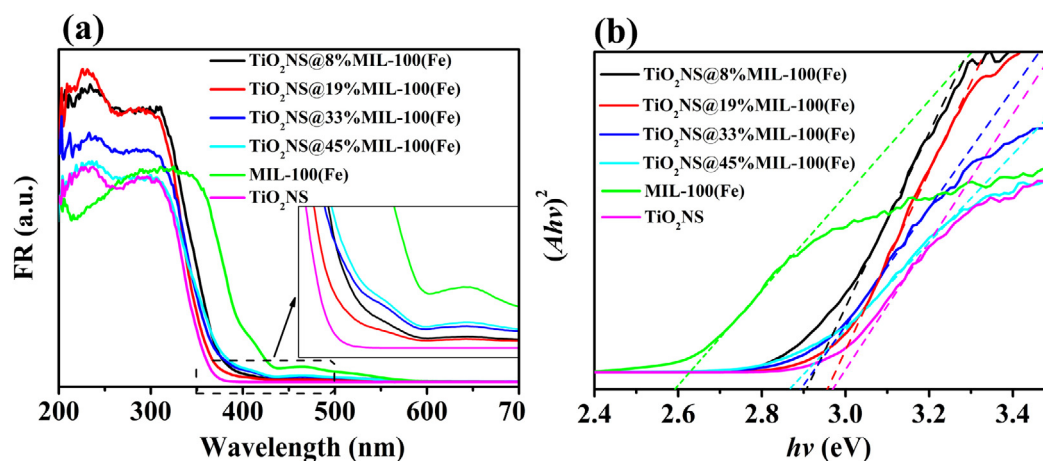
Fig. 6. (a) UV–vis DRS spectra of TiO$_2$NS, MIL-100(Fe) and TiO$_2$NS@MIL-100(Fe) nanocomposites; (b) plots of $(Ah\nu)^2$ as a function of $vs.$ photon energy of TiO$_2$NS, MIL-100(Fe) and TiO$_2$NS@MIL-100(Fe) nanocomposites.

photocatalytic reactions, the first-order model (Eq. (1)) is used to fit the experimental data.

$$-\ln\left(\frac{C_t}{C_0}\right) = kt \tag{1}$$

where λ is kinetic rate constant and was obtained from the adsorption and photocatalytic experiments. Kinetics of MB adsorption as a function of photocatalysts (Fig. 7b) reveals that pure MIL-100(Fe) exhibits the highest adsorption kinetic rate (0.034 min^{-1}) as a result of the largest functional surface area, which is in agreement with the BET results. Neat TiO$_2$NS adsorbs approximately 2% of MB owing to its layered structure with low adsorption capacity. Adsorption kinetic rates of the MIL-100(Fe)-TiO$_2$NS system increases with loaded quantity of MIL-100(Fe), which is attributed to the superior adsorption capacity of the photocatalysts with large surface area, offering appropriate reaction channels and facilitating the capture of organic molecules. Kinetics of MB degradation with respect to photocatalysts (Fig. 7c) demonstrates that TiO$_2$NS@33%MIL-100(Fe) displays the highest rate constant (0.045 min^{-1}), which is about 2 times larger than that for MIL-100(Fe) (0.019 min^{-1}), and 45 times larger than that for TiO$_2$NS (0.0008 min^{-1}) (Fig. 7d). This result is also consistent with the efficient separation of electron-hole pairs owing to the fast electron transfer between the interfaces of TiO$_2$NS and MIL-100(Fe). Notably, the photocatalytic performance of TiO$_2$NS@45%MIL-100(Fe) was found to be inefficient, which is most probably caused by the self-nucleation and

aggregation of MIL-100(Fe), reducing the photogenerated charges transfer between the interfaces. In order to further illustrate the integrative effect of TiO$_2$NS@MIL-100(Fe) nanocomposites photocatalytic reaction, TiO$_2$NS and MIL-100(Fe) were physically mixed with a weight proportion of 67:33 and exhibited a lower adsorption as well as photocatalytic property (Fig. S6).

Four circles of photodegradation of MB with TiO$_2$NS@33%MIL-100(Fe) nanocomposites under visible light were carried out to evaluate reusability. In each test, the suspension was placed in dark for 1 h to establish an adsorption–desorption equilibrium before irradiation. MB absorbance and decolorization during four consecutive circles confirms a good adsorption ability and slight deactivation of the as-prepared TiO$_2$NS@MIL-100(Fe) nanocomposites (Fig. 8). The slight decrease in photocatalytic efficiency may be incurred by the loss of the photocatalysts in centrifugation and washing process.

To better understand the effect of MIL-100(Fe) in the enhancement of the photoactivity of TiO$_2$NS@MIL-100(Fe) nanocomposites, Mott–Schottky measurements (Fig. S7) and photoluminescence emission spectra (PL) were performed for electrochemical analysis and measuring the efficiency of charge trapping and transfer, respectively. The flat-band potential of neat TiO$_2$NS determined from Mott–Schottky plots (Fig. S7a) is around −0.54 V $vs.$ Ag/AgCl, corresponding to −0.34 V $vs.$ the normal hydrogen electrode (NHE), while the flat-band potential of MIL-100(Fe) (Fig. S7b) is approximately −0.70 V $vs.$ Ag/AgCl, −0.50 V $vs.$ NHE. According to
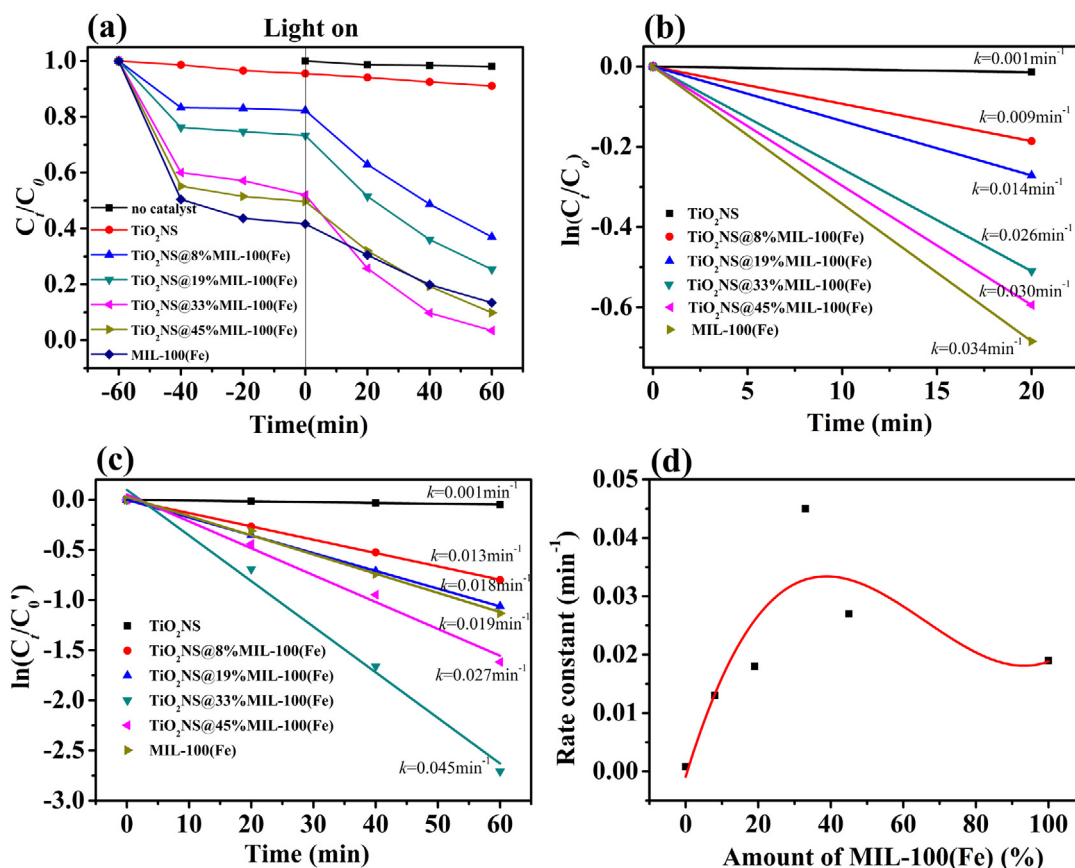
Fig. 7. (a) Control experiments of photodegradation of MB with respect to different photocatalysts under visible light ($\lambda \geq 420\,nm$); (b) kinetics of MB adsorption as a function of photocatalysts; (c) kinetics of MB degradation as a function of photocatalysts; (d) catalytic rate constant *vs.* weight ratio of MIL-100(Fe). C_t is the concentration of MB after adsorption and photocatalytic reactions, C_0 is the initial concentration of MB before dark adsorption, and C_0' is the concentration of MB before illumination. Reaction conditions: 20 mg photocatalyst, 100 ml of 50 mg l^{-1} MB aqueous solution and 0.2 ml H_2O_2.
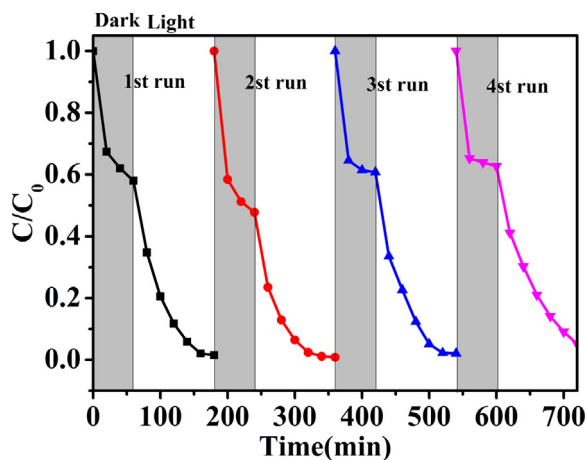

Fig. 8. Photocatalytic degradation of MB TiO$_2$NS@33%MIL-100(Fe) over four consecutive circles under visible light ($\lambda \geq 420\,nm$) with the H_2O_2 electron.

the band gap energy estimated from UV–vis DRS spectrum, the valence band potentials of TiO$_2$NS and MIL-100(Fe) are calculated to be 2.64 V and 2.08 V *vs.* NHE, respectively. The matched band potentials between TiO$_2$NS and MIL-100(Fe) make it theoretically feasible to transfer the photogenerated electrons from the conduction band (CB) of MIL-100(Fe) to the CB of TiO$_2$NS under visible light irradiation, which can lead to a effective separation of photogenerated electrons-holes pairs. This is also proved by the results of photocurrent transient response under intermittent
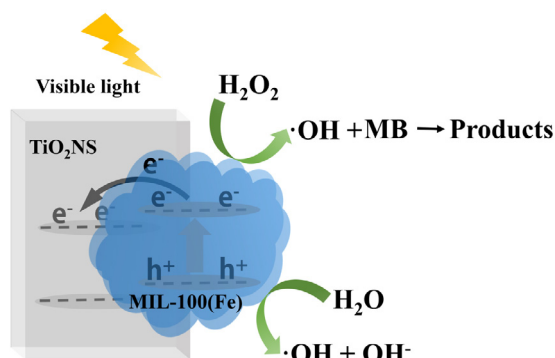
visible light irradiation ($\lambda \geq 420\,nm$) (Fig. 9a). It is obvious that the TiO$_2$NS@33%MIL-100(Fe) shows the strongest photocurrent intensity than that of MIL-100(Fe) and TiO$_2$NS, suggesting the most efficient separation of photoexcited electron-hole pairs owing to the fast electrons transfer from MIL-100(Fe) to TiO$_2$NS [32], which can be further confirmed by the PL results (Fig. 9b). The weakest PL spectra intensity of TiO$_2$NS@33%MIL-100(Fe) than that of neat TiO$_2$NS and pure MIL-100(Fe), indicates the lowest recombination rate of photoexcited electrons under an excitation wavelength of 250 nm [49].

According to the above results, a sound reaction mechanism for the photodegradation of MB over TiO$_2$NS@MIL-100(Fe) nanocomposites is postulated (Fig. 10). Under visible light illumination ($\lambda \geq 420\,nm$), the MIL-100(Fe) in TiO$_2$NS@MIL-100(Fe) nanocomposites is excited and generates electron-hole pairs. It is well acknowledged that charge transfer occurs between inorganic semiconductor and MOFs, and it substantially inhibits the electron-hole recombination [36]. Regarding TiO$_2$NS@MIL-100(Fe), the photoexcited electrons (e$^-$) transfer from valence band to conduction band on MIL-100(Fe) and holes (h$^+$) are produced in MIL-100(Fe)'s valence band. In addition, photo-excited electrons (e$^-$) transfer from conduction band of MIL-100(Fe) to that of TiO$_2$NS through the interaction between TiO$_2$NS and MIL-100(Fe), which suppresses the recombination of photogenerated electron-hole pairs and improves the efficiency of photocatalytic activity. The photoexcited holes (h$^+$) in the valence band of MIL-100(Fe) reacts directly with H_2O/OH$^-$ to generate hydrogen peroxide (•OH). Furthermore, it has been reported that the introduction of the hydrogen peroxide (H_2O_2) could facilitate photocatalytic reaction. As electron
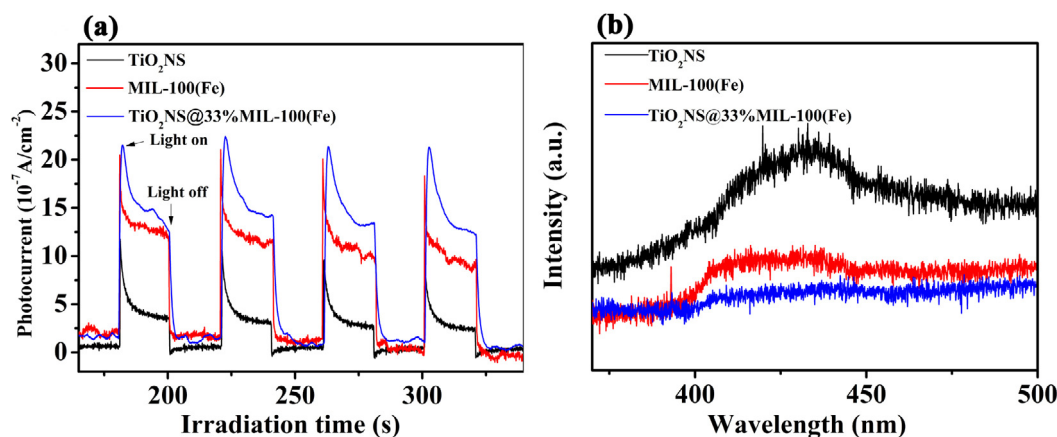
Fig. 9. (a) Transient photocurrent response of TiO_2NS, MIL-100(Fe), $TiO_2NS@33\%MIL-100(Fe)$ in 0.2 M Na_2SO_4 aqueous solution under intermittent visible light irradiation ($\lambda \geq 420$ nm). (b) PL spectra of TiO_2NS, MIL-100(Fe), $TiO_2NS@33\%MIL-100(Fe)$ with an excitation wavelength of 250 nm.

Fig. 10. Proposed mechanism for photocatalytic degradation of MB with $TiO_2NS@33\%MIL-100(Fe)$ under visible light irradiation ($\lambda \geq 420$ nm).

acceptor, H_2O_2 reacts with MIL-100(Fe) under visible light irradiation to produce a large number of $^\bullet OH$ radical groups [27,50–52]. As such, both the photogenerated holes (h^+) and the formed $^\bullet OH$ can directly oxidize the absorbed organic molecules [53].

4. Conclusion

In summary, hierarchical sandwich-like $TiO_2NS@MIL-100(Fe)$ nanocomposites were successfully prepared by incorporating inorganic semiconducting TiO_2NS with porous MIL-100(Fe). The as-prepared $TiO_2NS@MIL-100(Fe)$ nanocomposites exhibited excellent adsorption capacity and enhanced photocatalytic performance for the photodegradation of MB under visible light. The enhancement in photocatalytic activity can be attributed to the porous MIL-100(Fe) loading and the sandwich-like heterostructure which provides the platform for high-speed interfacial photogenerated charges transfer. We anticipate that our work could inspire the further exploration and utilization of MOFs and semiconductors nanocomposites.

Appendix A. Supplementary data

Supplementary material related to this article can be found, in the online version, at http://dx.doi.org/10.1016/j.apcatb.2017.02.073.

References

[1] Z. Zou, J. Ye, K. Sayama, H. Arakawa, Direct splitting of water under visible light irradiation with an oxide semiconductor photocatalyst, Nature 414 (2001) 625–627.

[2] S.U.M. Khan, M. Al-Shahry, W.B. Ingler, Efficient photochemical water splitting by a chemically modified n-TiO₂, Science 297 (2002) 2243.

[3] S. Liu, Z. Wang, C. Yu, H.B. Wu, G. Wang, Q. Dong, J. Qiu, A. Eychmüller, X.W. David Lou, A flexible TiO₂(B)-based battery electrode with superior power rate and ultralong cycle life, Adv. Mater. 25 (2013) 3462–3467.

[4] C. Wang, F. Wang, Y.J. Zhao, Y.H. Li, Q. Yue, Y.P. Liu, Y. Liu, A.A. Elzatahry, A. Al-Enizi, Y.P. Wu, Y.H. Deng, D.Y. Zhao, Hollow TiO₂₋ₓ porous microspheres composed of well-crystalline nanocrystals for high-performance lithium-ion batteries, Nano Res. 9 (2016) 165–173.

[5] H. Liu, W. Li, D. Shen, D. Zhao, G. Wang, Graphitic carbon conformal coating of mesoporous TiO₂ hollow spheres for high-performance lithium ion battery anodes, J. Am. Chem. Soc. 137 (2015) 13161–13166.

[6] C.B.D. Marien, T. Cottineau, D. Robert, P. Drogui, TiO₂ nanotube arrays: influence of tube length on the photocatalytic degradation of Paraquat, Appl. Catal. B: Environ. 194 (2016) 1–6.

[7] F. Cao, X. Jie, F. Wu, Q. Liu, Z. Shi, Y. Yu, X. Wang, L. Liang, Enhanced photoelectrochemical performance from rationally designed anatase/rutile TiO₂ heterostructures, ACS Appl. Mater. Interfaces 8 (2016) 12239–12245.

[8] V. Vaiano, G. Iervolino, D. Sannino, J.J. Murcia, M.C. Hidalgo, P. Ciambelli, J.A. Navío, Photocatalytic removal of patent blue V dye on Au-TiO₂ and Pt-TiO₂ catalysts, Appl. Catal. B: Environ. 188 (2016) 134–146.

[9] C. Hu, X. Zhang, W. Li, Y. Yan, G. Xi, H. Yang, J. Li, H. Bai, Large-scale, ultrathin and (001) facet exposed TiO₂ nanosheet superstructures and their applications in photocatalysis, J. Mater. Chem. A 2 (2014) 2040–2043.

[10] G. Xiang, T. Li, J. Zhuang, X. Wang, Large-scale synthesis of metastable TiO₂(B) nanosheets with atomic thickness and their photocatalytic properties, Chem. Commun. 46 (2010) 6801–6803.

[11] J. Yu, L. Qi, M. Jaroniec, Hydrogen production by photocatalytic water splitting over Pt/TiO₂ nanosheets with exposed (001) facets, J. Phys. Chem. C 114 (2010) 13118–13125.

[12] S. Wang, J.H. Yun, B. Luo, T. Butburee, P. Peerakiatkhajohn, S. Thaweesak, M. Xiao, L. Wang, Recent progress on visible light responsive heterojunctions for photocatalytic applications, J. Mater. Sci. Technol. 33 (2017) 1–22, http://dx.doi.org/10.1016/j.jmst.2016.1011.1017.

[13] D. Li, J. Jia, T. Zheng, X. Cheng, X. Yu, Construction and characterization of visible light active Pd nano-crystallite decorated and C-N-S-co-doped TiO₂ nanosheet array photoelectrode for enhanced photocatalytic degradation of acetylsalicylic acid, Appl. Catal. B: Environ. 188 (2016) 259–271.

[14] W. Guo, F. Zhang, C. Lin, Z.L. Wang, Direct growth of TiO₂ nanosheet arrays on carbon fibers for highly efficient photocatalytic degradation of methyl orange, Adv. Mater. 24 (2012) 4761–4764.

[15] W.S. Wang, D.H. Wang, W.G. Qu, L.Q. Lu, A.W. Xu, Large ultrathin anatase TiO₂ nanosheets with exposed {001} facets on graphene for enhanced visible light photocatalytic activity, J. Phys. Chem. C 116 (2012) 19893–19901.

[16] B.A. Al-Maythalony, O. Shekhah, R. Swaidan, Y. Belmabkhout, I. Pinnau, M. Eddaoudi, Quest for anionic MOF membranes: continuous sod-ZMOF

membrane with CO_2 adsorption-driven selectivity, J. Am. Chem. Soc. 137 (2015) 1754–1757.

[17] I. Spanopoulos, C. Tsangarakis, E. Klontzas, E. Tylianakis, G. Froudakis, K. Adil, Y. Belmabkhout, M. Eddaoudi, P.N. Trikalitis, Reticular synthesis of HKUST-like tbo MOFs with enhanced CH_4 storage, J. Am. Chem. Soc. 138 (2015) 12239–12245.

[18] Y.P. Yuan, L.S. Yin, S.W. Cao, G.S. Xu, C.H. Li, C. Xue, Improving photocatalytic hydrogen production of metal–organic framework UiO-66 octahedrons by dye-sensitization, Appl. Catal. B: Environ. 168 (2015) 572–576.

[19] I. Hod, M.D. Sampson, P. Deria, C.P. Kubiak, O.K. Farha, J.T. Hupp, Fe-porphyrin-based metal–organic framework films as high-surface concentration, heterogeneous catalysts for electrochemical reduction of CO_2, ACS Catal. 5 (2015) 6302–6309.

[20] M. Danhardi, C. Serre, T. Frot, L. Rozes, G. Maurin, C. Sanchez, G. Férey, A new photoactive crystalline highly porous titanium(IV) dicarboxylate, J. Am. Chem. Soc. 131 (2009) 10857–10859.

[21] S. Vaesen, V. Guillerm, Q. Yang, A.D. Wiersum, B. Marszalek, B. Gil, A. Vimont, M. Daturi, T. Devic, P.L. Llewellyn, A robust amino-functionalized titanium (IV) based MOF for improved separation of acid gases, Chem. Commun. 49 (2013) 10082–10084.

[22] Y. Fu, D. Sun, Y. Chen, R. Huang, Z. Ding, X. Fu, Z. Li, An amine-functionalized titanium metal–organic framework photocatalyst with visible-light-induced activity for CO_2 reduction, Angew. Chem. Int. Ed. 124 (2012) 3420–3423.

[23] D. Sun, L. Ye, Z. Li, Visible-light-assisted aerobic photocatalytic oxidation of amines to imines over NH_2-MIL-125 (Ti), Appl. Catal. B: Environ. 164 (2015) 428–432.

[24] K.G. Laurier, F. Vermoortele, R. Ameloot, D.E. De Vos, J. Hofkens, M.B. Roeffaers, Iron(III)-based metal–organic frameworks as visible light photocatalysts, J. Am. Chem. Soc. 135 (2013) 14488–14491.

[25] W.T. Xu, L. Ma, F. Ke, F.M. Peng, G.S. Xu, Y.H. Shen, J.F. Zhu, L.G. Qiu, Y.P. Yuan, Metal-organic frameworks MIL-88A hexagonal microrods as a new photocatalyst for efficient decolorization of methylene blue dye, Dalton Trans. 43 (2014) 3792–3798.

[26] D. Wang, R. Huang, W. Liu, D. Sun, Z. Li, Fe-based MOFs for photocatalytic CO_2 reduction: role of coordination unsaturated sites and dual excitation pathways, ACS Catal. 4 (2014) 4254–4260.

[27] D. Wang, M. Wang, Z. Li, Fe-based metal–organic frameworks for highly selective photocatalytic benzene hydroxylation to phenol, ACS Catal. 5 (2015) 6852–6857.

[28] H. Xu, J. Hu, D. Wang, Z. Li, Q. Zhang, Y. Luo, S. Yu, H. Jiang, Visible-light photoreduction of CO_2 in a metal–organic framework: boosting electron–hole separation via electron trap states, J. Am. Chem. Soc. 137 (2015) 13440–13443.

[29] C. Gomes Silva, I. Luz, F.X. Llabrés i Xamena, A. Corma, H. García, Water stable Zr-benzenedicarboxylate metal–organic frameworks as photocatalysts for hydrogen generation, Chem. Eur. J. 16 (2010) 11133–11138.

[30] D. Sun, Y. Fu, W. Liu, L. Ye, D. Wang, L. Yang, X. Fu, Z. Li, Studies on photocatalytic CO_2 reduction over NH_2-Uio-66 (Zr) and its derivatives: towards a better understanding of photocatalysis on metal-organic frameworks, Chem. Eur. J. 19 (2013) 14279–14285.

[31] D. Sun, W. Liu, M. Qiu, Y. Zhang, Z. Li, Introduction of a mediator for enhancing photocatalytic performance via post-synthetic metal exchange in metal–organic frameworks (MOFs), Chem. Commun. 51 (2015) 2056–2059.

[32] J.D. Xiao, Q. Shang, Y. Xiong, Q. Zhang, Y. Luo, S.H. Yu, H.L. Jiang, Boosting photocatalytic hydrogen production of a metal–organic framework decorated with platinum nanoparticles: the platinum location matters, Angew. Chem. Int. Ed. 128 (2016) 9535–9539.

[33] X. Zeng, L. Huang, C. Wang, J. Wang, J. Li, X. Luo, Sonocrystallization of ZIF-8 on electrostatic spinning TiO_2 nanofibers surface with enhanced photocatalysis property through synergistic effect, ACS Appl. Mater. Interfaces 8 (2016) 20274–20282.

[34] F. Ke, L. Wang, J. Zhu, Facile fabrication of CdS-metal-organic framework nanocomposites with enhanced visible-light photocatalytic activity for organic transformation, Nano Res. 8 (2015) 1834–1846.

[35] L. Shen, S. Liang, W. Wu, R. Liang, L. Wu, CdS-decorated UiO-66(NH_2) nanocomposites fabricated by a facile photodeposition process: an efficient and stable visible-light-driven photocatalyst for selective oxidation of alcohols, J. Mater. Chem. A 1 (2013) 11473–11482.

[36] J. He, Z. Yan, J. Wang, J. Xie, L. Jiang, Y. Shi, F. Yuan, F. Yu, Y. Sun, Significantly enhanced photocatalytic hydrogen evolution under visible light over CdS embedded on metal-organic frameworks, Chem. Commun. 49 (2013) 6761–6763.

[37] R. Li, J. Hu, M. Deng, H. Wang, X. Wang, Y. Hu, H.L. Jiang, J. Jiang, Q. Zhang, Y. Xie, Integration of an inorganic semiconductor with a metal–organic framework: a platform for enhanced gaseous photocatalytic reactions, Adv. Mater. 26 (2014) 4783–4788.

[38] S. Abedi, A. Morsali, Ordered mesoporous metal–organic frameworks incorporated with amorphous TiO_2 as photocatalyst for selective aerobic oxidation in sunlight irradiation, ACS Catal. 14 (1995) 47–70.

[39] G. Liu, H.G. Yang, J. Pan, Y.Q. Yang, G.Q. Lu, H.M. Cheng, Titanium dioxide crystals with tailored facets, Chem. Rev. 114 (2014) 9559–9612.

[40] B. Liu, Y. Huang, Y. Wen, L. Du, W. Zeng, Y. Shi, F. Zhang, G. Zhu, X. Xu, Y. Wang, Highly dispersive {001} facets-exposed nanocrystalline TiO_2 on high quality graphene as a high performance photocatalyst, J. Mater. Chem. 22 (2012) 7484–7491.

[41] X. Han, Q. Kuang, M. Jin, Z. Xie, L. Zheng, Synthesis of titania nanosheets with a high percentage of exposed (001) facets and related photocatalytic properties, J. Am. Chem. Soc. 131 (2009) 3152–3153.

[42] R. Canioni, C. RochMarchal, F. Secheresse, P. Horcajada, C. Serre, M. HardiDan, G. Ferey, J. Greneche, F. Lefebvre, J. Chang, Y. Hwang, O. Lebedev, S. Turner, G. Van Tendeloo, Stable polyoxometalate insertion within the mesoporous metal organic framework MIL-100(Fe), J. Mater. Chem. 21 (2011) 1226–1233.

[43] F. Ke, L. Qiu, Y. Yuan, X. Jiang, J. Zhu, Fe_3O_4@MOF core-shell magnetic microspheres with a designable metal–organic framework shell, J. Mater. Chem. 22 (2012) 9497–9500.

[44] N.U. Qadir, S.A.M. Said, R.B. Mansour, K. Mezghani, A. Ul-Hamid, Synthesis, characterization, and water adsorption properties of a novel multi-walled carbon nanotube/MIL-100(Fe) composite, Dalton Trans. 45 (2016) 15621–15633.

[45] S.J. Yang, J.H. Im, T. Kim, K. Lee, C.R. Park, MOF-derived ZnO and ZnO@C composites with high photocatalytic activity and adsorption capacity, J. Hazard. Mater. 186 (2011) 376–382.

[46] H.G. Yang, C.H. Sun, S.Z. Qiao, J. Zou, G. Liu, S.C. Smith, H.M. Cheng, G.Q. Lu, Anatase TiO_2 single crystals with a large percentage of reactive facets, Nature 453 (2008) 638–641.

[47] Z. Sun, T. Liao, Y. Dou, S.M. Hwang, M.-S. Park, L. Jiang, J.H. Kim, S.X. Dou, Generalized self-assembly of scalable two-dimensional transition metal oxide nanosheets, Nat. Commun. 5 (2014) 3813–3841.

[48] F. Ke, L. Qiu, J. Zhu, Fe_3O_4@MOF core-shell magnetic microspheres as excellent catalysts for the Claisen-Schmidt condensation reaction, Nanoscale 6 (2014) 1596–1601.

[49] W. Yao, Y. Li, D. Yan, M. Ma, Z. He, S. Chai, X. Su, F. Chen, Q. Fu, Fabrication and photocatalysis of TiO_2-graphene sandwich nanosheets with smooth surface and controlled thickness, Chem. Eng. J. 229 (2013) 569–576.

[50] J. Du, Y. Yuan, J. Sun, F. Peng, X. Jiang, L. Qiu, A. Xie, Y. Shen, J. Zhu, New photocatalysts based on MIL-53 metal–organic frameworks for the decolorization of methylene blue dye, J. Hazard. Mater. 190 (2011) 945–951.

[51] L. Ai, C. Zhang, L. Li, J. Jiang, Iron terephthalate metal–organic framework: revealing the effective activation of hydrogen peroxide for the degradation of organic dye under visible light irradiation, Appl. Catal. B: Environ. 148–149 (2014) 191–200.

[52] R. Liang, L. Shen, F. Jing, W. Wu, Q. Na, L. Rui, W. Ling, M@MIL-100(Fe) (M = Au, Pd, Pt) nanocomposites fabricated by a facile photodeposition process: efficient visible-light photocatalysts for redox reactions in water, Nano Res. 162 (2015) 245–251.

[53] C. Zhang, L. Qiu, F. Ke, Y. Zhu, Y. Yuan, G. Xu, X. Jiang, A novel magnetic recyclable photocatalyst based on a core-shell metal-organic framework Fe_3O_4@MIL-100(Fe) for the decolorization of methylene blue dye, J. Mater. Chem. A 1 (2013) 14329–14334.